Chinese Chemical Letters 37 (2026) 110952

Contents lists available at ScienceDirect

Chinese Chemical Letters

journal homepage: www.elsevier.com/locate/cclet

Intelligent structure modulator for enhancing wide-temperature compatibility of aqueous zinc-ion batteries

Xiaoxi Zhao[a,c], Qingyun Dou[b,*], Bingjun Yang[a,c,*], Qunji Xue[a,*], Xingbin Yan[b]

[a] Research Center of Resource Chemistry and Energy Materials, State Key Laboratory of Solid Lubrication, Lanzhou Institute of Chemical Physics, Chinese Academy of Sciences, Lanzhou 730000, China
[b] School of Materials Science and Engineering, Sun Yat-sen University, Guangzhou 510275, China
[c] Center of Materials Science and Optoelectronics Engineering, University of Chinese Academy of Sciences, Beijing 100049, China

ARTICLE INFO

Article history:
Received 16 December 2024
Revised 19 January 2025
Accepted 12 February 2025
Available online 13 February 2025

Keywords:
Poloxamer 407 (P407)
Electrolyte modification
Solid electrolyte interphase
Thermoreversible gelation
Wide-temperature adaptability
Aqueous zinc-ion batteries

ABSTRACT

Aqueous zinc-ion batteries (AZIBs) are the low-cost and safe secondary battery technology with great application prospects, but remain hindered by the severe Zn-electrolyte interface compatibility, especially in extreme environmental temperature. Innovative electrolyte design is the key to solving the above problems. Here, we introduce an electrolyte additive of Poloxamer 407 (P407) as a solvation restructuring agent and H_2O cluster modulator, effectively stabilizing H_2O molecules and suppressing parasitic reactions. Meanwhile, P407 facilitates the formation of a stable solid electrolyte interphase (SEI) composed of organic-inorganic composite, thereby improving the interfacial chemistry. More importantly, the thermoreversible gelation property of P407 enhances the system's high-temperature stability by forming micelle network structures that effectively retains H_2O molecules, while at low temperature, it maintains the fluidity of the electrolyte, ensuring efficient ion transport. By using P407-containing electrolyte, the Zn anode achieves long cycling life of 4000, 850, and 1000 h at 30, 60 and −30 °C, respectively. Moreover, the modified electrolyte enables the Zn-V_2O_5 full cells to achieve excellent rate performance and cycling stability in a wide temperature range from −30 °C to 60 °C. This study highlights a simple yet effective strategy for electrolyte modification using P407, providing a pathway toward the development of high-performance AZIBs with broad temperature adaptability.

© 2026 Published by Elsevier B.V. on behalf of Chinese Chemical Society and Institute of Materia Medica, Chinese Academy of Medical Sciences.

Aqueous zinc-ion batteries (AZIBs) are regarded as promising candidates for large-scale energy storage owing to their affordability, safety, environmental sustainability, as well as a high theoretical specific capacity (820 mAh/g and 5855 mAh/cm^3) and a low redox potential (−0.76 V *vs.* standard hydrogen electrode) of the Zn anodes [1–3]. However, the high reactivity of solvent H_2O leads to severe hydrogen evolution reactions (HER) on the Zn anode surface, which further exacerbates interface corrosion, by-product formation, and Zn dendrite growth, collectively degrading battery performance [4–7]. What is more, stable operation of AZIBs under extreme temperatures is a huge challenge [8,9]. Specifically, high temperature can accelerate thermodynamic and kinetic processes, intensifying water evaporation and side reactions; while low temperature can impede ion transport, resulting in compromising the electrochemical performance of AZIBs.

Achieving wide-temperature performance for AZIBs is essential for their practical large-scale applications. This requires suppressing the inherent H_2O activity in aqueous electrolytes not at the price of a decrease in ion transport [10]. To this end, several electrolyte engineering strategies have been proposed, including high-concentration electrolytes, solid or quasi-solid electrolytes, organic-inorganic hybrid electrolytes, and additive strategies [11,12]. High-concentration electrolytes with limited free H_2O can inhibit HER by high salt/H_2O molar ratio, while these electrolytes suffer from high viscosity of limited ion transport especially at low temperature [13–15]. Solid or quasi-solid electrolytes provide physical barriers against leakage and suppress Zn dendrite formation, but their low ionic conductivity and interfacial resistance limit high-rate performance [16–18]. Although organic-aqueous hybrid electrolytes exhibit broadened electrochemical stability window and enhanced wide-temperature performance, hybrid formulations including organic solvents add to costs, increase flammability, and would reduce stability at high temperature [19,20].

In comparison, the electrolyte additive strategy is regarded as a promising approach thanks to its advantages of simplicity,

* Corresponding authors.
E-mail addresses: douqy3@mail.sysu.edu.cn (Q. Dou), yangbj@licp.cas.cn (B. Yang), qjxue@nimte.ac.cn (Q. Xue).

https://doi.org/10.1016/j.cclet.2025.110952
1001-8417/© 2026 Published by Elsevier B.V. on behalf of Chinese Chemical Society and Institute of Materia Medica, Chinese Academy of Medical Sciences.

operability, and cost-effectiveness. Electrolyte additives in AZIBs perform multiple functions, including regulating solvation structures, altering hydrogen bond (HB) networks, forming adsorption layers, generating electrostatic shielding effects, and constructing the SEIs [21–24]. Although additive engineering has significantly enhanced the performance of AZIBs, there remains a need to develop additives that can broaden the operational temperature range of the electrolytes [25]. At high temperature, water evaporation and increased side reactions compromise the cycling stability of the Zn anodes; this issue can be addressed by forming gel structures within the electrolyte that restrict water migration [26,27]. Conversely, in environments below 0 °C, traditional aqueous electrolytes tend to freeze, leading to reduced ion transport and sluggish electrochemical kinetics. Maintaining the electrolyte in a liquid state under low temperature can mitigate these problems [28–30]. Therefore, achieving a wide-temperature operational system requires ensuring stability at high temperature while maintaining efficient ion conduction at low temperature. Introducing an additive that makes electrolyte remain liquid at low temperature and transition to a gel state at high temperature can simultaneously satisfy performance requirements under both conditions. Hence, thermosensitive polymers are undoubtedly excellent candidates for this role.

Herein, a thermosensitive nonionic surfactant, poloxamer 407 (P407), is introduced into a zinc trifluoromethanesulfonate ($Zn(OTf)_2$)-based aqueous electrolyte. At room temperature, P407 acts as a solvation restructuring agent and H_2O cluster modulator, facilitating the incorporation of both P407 and OTf^- into the Zn^{2+} solvation shell and reconstructing the HB network *via* H_2O and P407 interactions. This enhances the stability of H_2O, reduces parasitic reactions, and promotes the formation of an organic-inorganic composite SEI layer arising from P407 and OTf^- decomposition. Benefiting from these improvements, with P407-containing electrolyte, the Zn||Zn symmetric cell cycles stably for 4000 h at 1 mA/cm^2, the Zn||Cu cell achieves coulombic efficiency (CE) of 99.2 %, and the Zn-V_2O_5 full cell delivers 114.2 mAh/g at 10 A/g, retaining 94.2 % after 6000 cycles at 30 °C. Notably, electrolyte containing an appropriate concentration P407 remains in a liquid state at room and low temperatures, ensuring efficient ion transport. At high temperature, the micelles intertwine and crosslink to form network structure, effectively trapping H_2O molecules to prevent evaporation and maintain normal battery operation [31]. This unique thermosensitive property enables modified electrolyte to exhibit excellent reversibility and stability across a wide temperature range from −30 °C to 60 °C. Moreover, the cycling performance of the full cell is significantly enhanced, highlighting its potential as a promising wide-temperature electrolyte for AZIBs.

A series of electrolytes were prepared by adding P407 of different mass concentrations (10 wt%, 20 wt%, and 30 wt%) into 2 mol/L $Zn(OTf)_2$ aqueous electrolyte. The 2 mol/L $Zn(OTf)_2$ aqueous electrolyte and P407-modified $Zn(OTf)_2$ electrolytes are denoted as $Zn(OTf)_2/H_2O$ and P407-$Zn(OTf)_2/H_2O$, respectively.

The intermolecular interactions within the electrolytes were systematically investigated using various spectroscopic techniques. Figs. 1a and b revealed nuclear magnetic resonance (NMR) spectra [32,33]. When P407 was added to the $Zn(OTf)_2/H_2O$, the ^{1}H NMR peak of H_2O molecules gradually shifted downfield from 4.735 ppm to 4.744 ppm, which indicated a decrease in electron cloud density around the hydrogen atoms of H_2O arising from their HB interactions with P407. Additionally, the ^{19}F NMR peak of OTf^- anions shifted downfield from −79.752 ppm (in $Zn(OTf)_2/H_2O$) to −79.593 ppm (in 30 % P407-$Zn(OTf)_2/H_2O$), which is attributed to an enhanced pairing interaction between OTf^- and Zn^{2+} in the P407-$Zn(OTf)_2/H_2O$.

Fourier-transform infrared (FTIR) spectroscopy further elucidated the interactions among electrolyte components and the evolution of Zn^{2+} solvation environments [34]. As depicted in Fig. 1c and Fig. S1 (Supporting information), the O−H stretching vibration in $Zn(OTf)_2/H_2O$ appeared as a broad band in the 3000−3800 cm^{-1} range, corresponding to three distinct states of H_2O molecules: Network water (NW) at around 3205 cm^{-1}, intermediate water (IW) at around 3412 cm^{-1}, and multiple water (MW) at around 3564 cm^{-1} [35]. As P407 concentration increased, the proportion of NW decreased significantly, implying that the introduction of P407 disrupted the strong HB network among H_2O molecules while strengthening HB between P407 and H_2O. Additionally, a blue shift in the O−H bending vibration in the 1600−1700 cm^{-1} range suggested the formation of HB between P407 and H_2O (Fig. S2a in Supporting information). To exclude the influence of Zn^{2+}, FTIR spectra were also recorded for P407/H_2O solutions without zinc salts (Fig. S3 in Supporting information). The results demonstrated that, as the P407 concentration increased, the O−H bending vibration peak shifted to higher wavenumbers, confirming the interaction between P407 and H_2O. This reconstructed strong HB network reduced H_2O activity, beneficial for suppressing HER and associated side reactions. In addition, as shown in Fig. 1d, the S=O stretching vibration of OTf^- around 1028 cm^{-1} exhibited a blue shift upon P407 addition, indicating that P407 could modulate the coordination environment of OTf^-. The changes in the S=O and C−F bond vibrations further indicated that P407 allowed the incorporation of OTf^- into the Zn^{2+} solvation sheath. Additionally, Raman spectra further confirmed these findings, showing similar trends in the vibration changes of the S=O and C−F bonds (Fig. 1e, Figs. S2b and S4 in Supporting information). Moreover, the gradual introduction of P407 to the $Zn(OTf)_2/H_2O$ system resulted in a red shift of the C−O stretching vibration of P407 (Fig. 1f), suggesting that P407 was incorporated into the Zn^{2+} solvation sheath. The overall data indicated that P407 led to forming a new HB network with H_2O molecules, meanwhile, replacing some coordinated H_2O molecules and constructing a stable composite solvation sheath consisting of P407, OTf^-, and H_2O.

To gain deeper insights of the influence of P407 on the solvation structure of Zn^{2+}, molecular dynamics (MD) simulations were performed for two different electrolyte systems [36]. As depicted in Fig. S5 (Supporting information), the $Zn(OTf)_2/H_2O$ initially contained six H_2O molecules in the primary solvation shell (PSS) of Zn^{2+}. However, in the 20 % P407-$Zn(OTf)_2/H_2O$, both OTf^- and P407 partially replaced H_2O molecules in the Zn^{2+}-PSS (Fig. 1g). Radial distribution functions (RDFs) showed that in the 20 % P407-$Zn(OTf)_2/H_2O$ electrolyte, three Zn^{2+}−O peaks corresponding to H_2O, OTf^- and P407 appeared around 2.08 Å. The average coordination numbers of Zn^{2+} with H_2O, OTf^-, and P407 in the Zn^{2+}−PSS were 3.97, 0.96, and 1.02, respectively (Fig. 1h). These findings confirmed that the introduction of P407 significantly altered the Zn^{2+} solvation structure, resulting in a reduction in solvated H_2O content. This restructured solvation configuration decreased H_2O activity, which was crucial for suppressing HER and improving electrochemical performance. Furthermore, the incorporation of anion and organic molecule into the Zn^{2+} solvation shell facilitated the formation of SEI during the Zn plating process, as detailed in the following sections.

The P407 additive significantly mitigated side reactions on the Zn foil surface prior to cell operation. It was revealed that after 5 days of immersion in $Zn(OTf)_2/H_2O$ electrolyte, the Zn foil surface was severely corroded and covered with by-products. In contrast, the Zn foil soaked in 20 % P407-$Zn(OTf)_2/H_2O$ electrolyte retained a smooth surface with trace residues, highlighting P407's role in stabilizing Zn foil and reducing pre-operational degradation (Fig. S6 in Supporting information) [37]. To evaluate the impact of P407 on battery performance, electrochemical measurements were conducted using Zn||Zn symmetric and Zn||Cu asymmetric

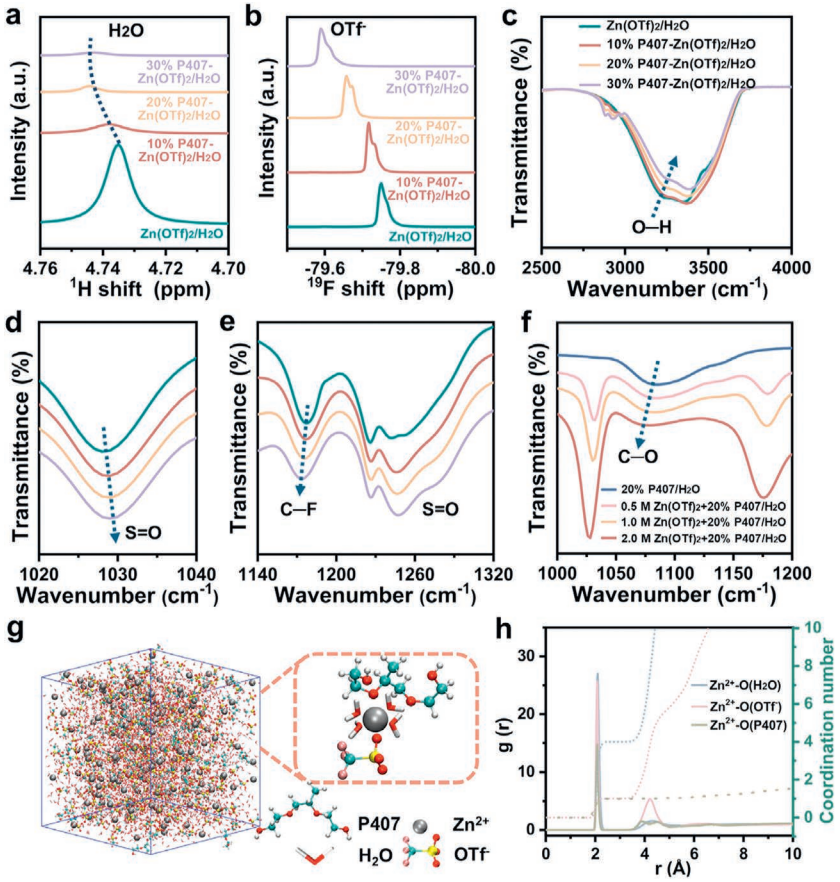


Fig. 1. Analysis of intermolecular interactions in electrolytes. (a) ^{1}H NMR and (b) ^{19}F NMR spectra of different electrolytes. FTIR spectra of different electrolytes (c) between 2500 cm^{-1} and 4000 cm^{-1}, (d) between 1020 cm^{-1} and 1040 cm^{-1}, and (e) between 1140 cm^{-1} and 1320 cm^{-1}. (f) FTIR spectra of electrolytes with different concentrations of $Zn(OTf)_2$ added to 20% P407/H_2O. (g) MD simulation snapshot and (h) RDFs and the corresponding coordination numbers in 20% P407-$Zn(OTf)_2/H_2O$.

cells. The optimal P407 concentration in $Zn(OTf)_2/H_2O$ was 20%, which provided the best electrochemical stability (Fig. S7 in Supporting information). Fig. 2a showed the galvanostatic cycling performance of Zn||Zn symmetric cells in $Zn(OTf)_2/H_2O$ and 20% P407-$Zn(OTf)_2/H_2O$ electrolytes. At 1 mA/cm^2 and 1 mAh/cm^2, the introduction of P407 significantly improved the cycling stability, allowing the cell to operate for over 4000 h without noticeable voltage hysteresis, greatly outperforming the $Zn(OTf)_2/H_2O$, which failed after 100 h. The time-voltage profile further verified the stable operation of the cell during long-term plating/stripping processes (insets in Fig. 2a). Additionally, the introduction of P407 increased the Zn^{2+} plating/stripping potential, primarily due to a reduction in ionic conductivity (Fig. S8 in Supporting information). Even at a higher current density of 3 mA/cm^2, the Zn||Zn symmetric cell with 20% P407-$Zn(OTf)_2/H_2O$ exhibited stable cycling for over 1800 h, while the cell with $Zn(OTf)_2/H_2O$ failed after approximately 20 h (Fig. 2b). Importantly, at more demanding conditions (5 mA/cm^2 and 5 mAh/cm^2), the Zn||Zn symmetric cell with 20% P407-$Zn(OTf)_2/H_2O$ still maintained stable operation for up to 500 h, as shown in Fig. S9 (Supporting information), demonstrating its great potential for practical applications.

Subsequently, Zn||Cu asymmetric cells were tested to evaluate the reversibility of Zn deposition/stripping. At 2 mA/cm^2 and 1 mAh/cm^2, the Zn||Cu cell with $Zn(OTf)_2/H_2O$ short-circuited after 50 cycles, whereas the cell with 20% P407-$Zn(OTf)_2/H_2O$ exhibited significantly improved stability, with a cycling lifespan exceeding 450 cycles (Fig. 2c). The cell with 20% P407-$Zn(OTf)_2/H_2O$ maintained a high CE of 99.2% after 450 cycles (Fig. 2d), while the cell with $Zn(OTf)_2/H_2O$ failed prematurely (Fig. 2e). Even under higher current density (4 mA/cm^2) and capacity (2 mAh/cm^2), the reversibility of Zn deposition/stripping remained excellent, achieving over 300 cycles with an average CE of 99.1% (Fig. S10 in Supporting information). Moreover, the introduction of P407 also significantly enhanced the rate performance of Zn||Zn symmetric cells (Fig. 2f and Fig. S11 in Supporting information). The cell with $Zn(OTf)_2/H_2O$ short-circuited when the current density increased to 5 mA/cm^2, whereas the cell with 20% P407-$Zn(OTf)_2/H_2O$ consistently exhibited stable voltage polarization and excellent rate performance.

The introduction of P407 reduced H_2O activity, and its effect on HER suppression was investigated using linear sweep voltammetry (LSV). As shown in Fig. 2g, the addition of 20% P407 to the $Zn(OTf)_2/H_2O$ significantly broadened the voltage window, which indicated effective HER inhibition. The superiority of the P407 additive was also manifested by the Tafel plots (Fig. S12 in Supporting information). Adding P407 to $Zn(OTf)_2/H_2O$ electrolyte reduced the corrosion current of Zn and increased the corrosion potential from −0.897 V to −0.894 V, indicating improved compatibility and less corrosion on the Zn anode. Additionally, the nucleation overpotential in Zn||Cu asymmetric cells using 20% P407-$Zn(OTf)_2/H_2O$ shifted to a more negative value (Fig. 2h). This shift indicated that P407 facilitated the Zn deposition layer with smaller grain sizes, which enhanced the deposition stability [38]. Such results ultimately contributed to a dendrite-free Zn anode, enhancing both performance and safety.

To evaluate the effect of the modified electrolyte on Zn deposition and Zn anode protection, the morphological evolution of Zn anodes was characterized using scanning electron microscopy

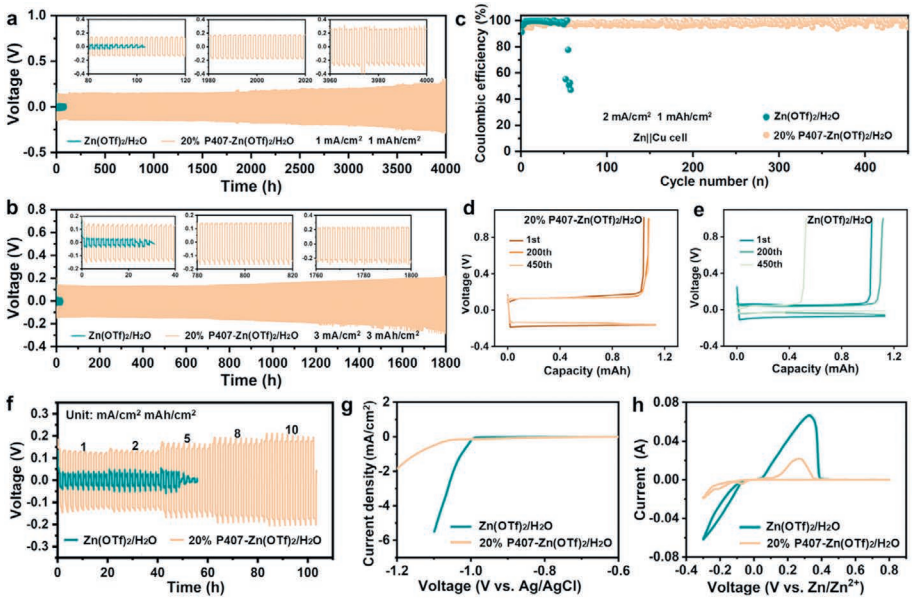


Fig. 2. Electrochemical performance of Zn anodes. Long-term constant current cycling performance of Zn||Zn symmetric cells using two electrolytes at (a) 1 mA/cm^2 and 1 mAh/cm^2, and (b) 3 mA/cm^2 and 3 mAh/cm^2. Insets show magnified views of the voltage profiles. (c) CE of Zn deposition/stripping in Zn||Cu asymmetric cells using two electrolytes at 2 mA/cm^2 and 1 mAh/cm^2. The corresponding voltage curves at different cycle numbers in Zn||Cu asymmetric cells using (d) 20 % P407-Zn(OTf)$_2$/H$_2$O and (e) Zn(OTf)$_2$/H$_2$O electrolytes. (f) Rate performance of Zn||Zn symmetric cells using two electrolytes at current densities from 1 mA/cm^2 to 10 mA/cm^2. (g) LSV curves of two electrolytes. (h) CV curves showing Zn nucleation behavior on Cu cathodes in Zn||Cu asymmetric cells in two electrolytes.

(SEM), atomic force microscopy (AFM), and 3D digital microscopy. After 50 cycles, Zn deposits in the Zn(OTf)$_2$/H$_2$O exhibited uneven distribution, with sheet-like dendrites and hexagonal by-products (Fig. 3a). In contrast, Zn anode in the 20 % P407-Zn(OTf)$_2$/H$_2$O displayed a smooth, dendrite-free surface with minimal signs of corrosion (Fig. 3b). Furthermore, AFM analysis revealed significant surface roughness in Zn(OTf)$_2$/H$_2$O due to severe dendrite growth, whereas 20 % P407-Zn(OTf)$_2$/H$_2$O resulted in minor protrusions and reduced roughness (Figs. 3c and d, Fig. S13 in Supporting information) [39]. These findings demonstrated that the introduction of P407 effectively suppressed Zn dendrite growth, promoting a more stable and uniform Zn anode morphology.

To further investigate interfacial chemical characteristics, Ar$^+$ sputtering *X*−ray photoelectron spectroscopy (XPS) was used to analyze Zn anodes after 20 cycles in the two electrolytes. Before sputtering, the SEI layers in both electrolytes contained −CF$_3$ and −SO$_3$ components, originating from the partial decomposition of OTf$^-$ or trace salt residues. As shown in Figs. 3e and j, as sputtering proceeded, F 1s spectra (~684.2 eV) revealed significantly higher ZnF$_2$ content in the SEI formed in 20 % P407-Zn(OTf)$_2$/H$_2$O, indicating a denser and more uniform structure compared to that in Zn(OTf)$_2$/H$_2$O. Meanwhile, the S 2p spectrum revealed the presence of ZnS (~161.5 eV) and ZnSO$_3$ (~168.0 eV) as the main components of the SEI in 20 % P407-Zn(OTf)$_2$/H$_2$O, while Zn(OTf)$_2$/H$_2$O showed a substantial decrease in the ZnS signal with sputtering (Figs. 3f and k). This related to the solvation structure of 20 % P407-Zn(OTf)$_2$/H$_2$O, where OTf$^-$ integrated into the solvation shell and decomposed at the Zn-electrolyte interface, forming these components. The higher ZnF$_2$ and ZnS content contributed to enhanced corrosion resistance [40]. The O 1s spectra highlighted differences in stability between the SEI layers. In Zn(OTf)$_2$/H$_2$O, the high Zn(OH)$_2$/ZnO content indicated that irreversible side reactions hindered SEI stability (Fig. 3g). Conversely, 20 % P407-Zn(OTf)$_2$/H$_2$O resulted in significantly lower Zn(OH)$_2$/ZnO content, forming a more robust and stable SEI (Fig. 3l). Moreover, as shown in Figs. 3h and m, Zn 2p spectra also showed higher Zn^{2+} content in the SEI of the 20 % P407-Zn(OTf)$_2$/H$_2$O, suggesting a dense, uniform SEI enriched with a substantial amount of zinc compounds. Additionally, C 1s spectra identified organic components, including C−H/C−C, C−S/C−O, and ZnCO$_3$, derived from the electrochemical decomposition of P407 and OTf$^-$ (Figs. 3i and n). These organic materials were concentrated at the SEI surface and diminished rapidly with sputtering, suggesting that these materials were primarily localized at the SEI surface.

Additionally, XRD analysis was employed to investigate the crystallographic difference of the deposited Zn products in the two electrolytes (Fig. 3o). In Zn(OTf)$_2$/H$_2$O, Zn deposition showed no clear preference for orientation, while Zn deposition in 20 % P407-Zn(OTf)$_2$/H$_2$O exhibited a significantly enhanced (002) peak. Quantitative analysis showed that the $I_{(002)}/I_{(100)}$ ratio increased from 0.87 to 5.74, indicating a preferential Zn deposition along the (002) crystal plane in the 20 % P407-Zn(OTf)$_2$/H$_2$O. This suggested that the organic-inorganic hybrid SEI layer formed a stable interface that promoted Zn deposition and preferential growth of the (002) crystal plane [41]. This preferential orientation along the (002) plane facilitated uniform Zn deposition [42], resulting in a smooth, dendrite-free surface, as observed in the SEM images. In conclusion, Zn(OTf)$_2$/H$_2$O resulted in severe dendrite growth, uneven morphology, and an unstable SEI dominated by Zn(OH)$_2$/ZnO. However, the solvation structure of the 20 % P407-Zn(OTf)$_2$/H$_2$O electrolyte led to the decomposition of P407 and the OTf$^-$, resulting in the *in situ* formation of a hybrid SEI with an organic-rich outer layer and an inorganic-rich inner layer comprising ZnF$_2$ and ZnS. This hybrid structure ensured uniform Zn deposition, enhanced stability, and better cycling performance (Fig. 3p).

Interestingly, P407 exhibits thermoreversible gelation properties. As shown in Fig. 4a, P407 is a block copolymer containing hydrophilic polyethylene glycol (PEO) segments and hydrophobic polypropylene glycol (PPO) segments. This structure allows P407 to transition between liquid and gel states with temperature changes. At low temperature, P407 aggregates into micelles, with PEO segments forming HB with H$_2$O molecules, thereby maintaining the system in a liquid state. As the temperature increases, these HB break, and PPO segments aggregate into a network structure *via* hydrophobic interactions, thus transforming into a gel [43]. Experiments were conducted to evaluate the phase states of the

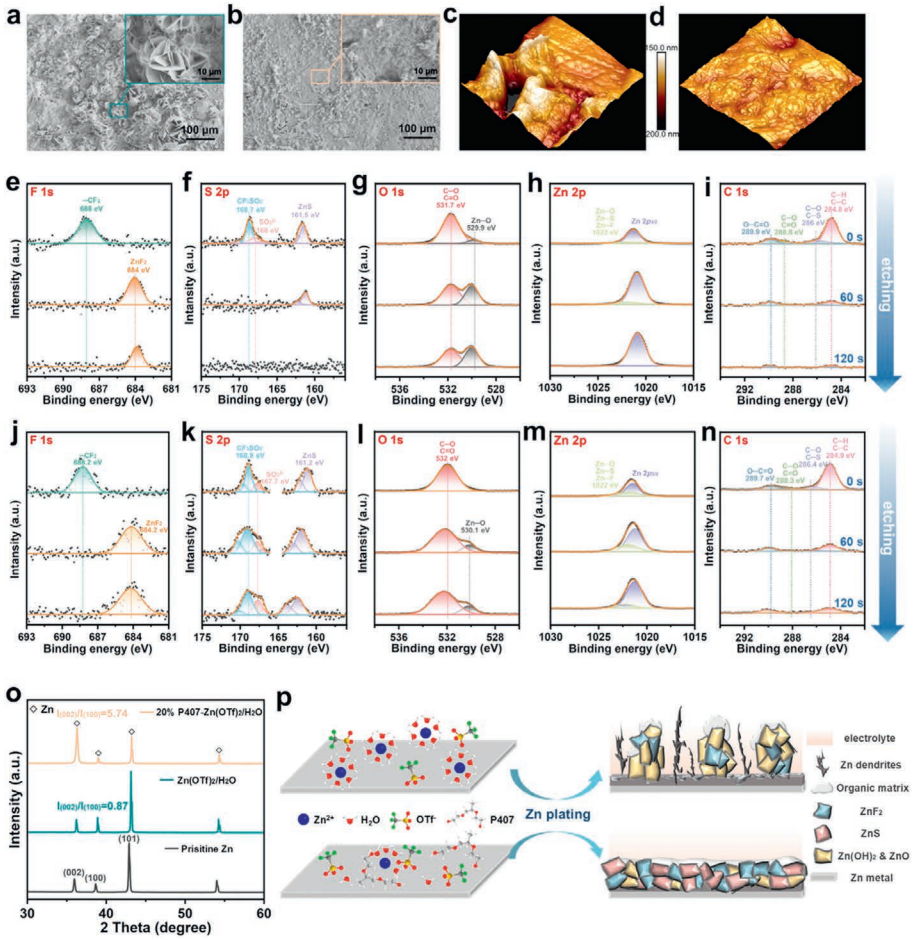


Fig. 3. Structural evolution of Zn anodes and interface chemistry. (a, b) SEM and (c, d) AFM images of Zn anodes after cycling for 100 h at 1 mA/cm^2 and 1 mAh/cm^2 in two electrolytes. XPS spectra of the cycled Zn anodes (e–i) in $Zn(OTf)_2/H_2O$ and (j–n) in 20% P407-$Zn(OTf)_2/H_2O$. (o) XRD pattern of the cycled Zn anodes in two electrolytes. (p) Dendrites and side reactions on the Zn anode in $Zn(OTf)_2/H_2O$ and SEI of Zn anode in 20% P407-$Zn(OTf)_2/H_2O$.

20% P407-$Zn(OTf)_2/H_2O$ electrolyte at room and high temperatures. As shown in Fig. S14 (Supporting information), the liquid electrolyte transitioned into a gel as the temperature increased from room temperature to 90 °C. This result confirmed that the 20% P407-$Zn(OTf)_2/H_2O$ electrolyte retained the thermosensitive properties. At low temperature, as illustrated in Fig. 4b, the electrolyte remained in solution, allowing molecules to migrate freely. At higher temperature, the formed network structures immobilized H_2O, enhancing the electrolyte's thermal adaptability by restricting molecular movement. In the high-temperature water retention experiment, the water in $Zn(OTf)_2/H_2O$ gradually evaporated over time, leaving only zinc salt solids behind. In contrast, 20% P407-$Zn(OTf)_2/H_2O$ retained water consistently and stably over an extended period, allowing it to continue operating normally at high temperatures (Fig. 4c). At −30 °C, $Zn(OTf)_2/H_2O$ and 20% P407-$Zn(OTf)_2/H_2O$ electrolytes remained in a liquid state without freezing (Fig. S15 in Supporting information), indicating good ionic conductivities under low temperatures. This allowed 20% P407-$Zn(OTf)_2/H_2O$ stable operation over a wide temperature range. For comparison, polyethylene glycol (PEG), which only contained ethylene glycol segments with a similar molecular weight as P407 was added to $Zn(OTf)_2/H_2O$ electrolyte. As shown in Fig. S16 (Supporting information) and Fig. 4g, both P407 and PEG produced similar effects on the electrochemical performance of the electrolytes, resulting in comparable cycling stability at 30 °C and −30 °C. However, at 60 °C, the 20% P407-$Zn(OTf)_2/H_2O$ electrolyte demonstrated superior electrochemical stability and much longer cycle life than 20% PEG-$Zn(OTf)_2/H_2O$ electrolyte (Fig. 4d). This result could be attributed to that PEG lacked thermoreversible gelation properties, resulting in a markedly different H_2O behavior in the 20% PEG-$Zn(OTf)_2/H_2O$ (Fig. S17 in Supporting information). At low temperature, H_2O molecules exhibited low kinetic energy, while at higher temperature, the molecules became more active and more prone to evaporation. As a result, the 20% P407-$Zn(OTf)_2/H_2O$ electrolyte exhibited greater stability and less molecular motion at high temperature compared to the 20% PEG-$Zn(OTf)_2/H_2O$ electrolyte, confirming the stabilizing effect of P407. To ensure the rigor of our conclusions, we also selected a polymer containing PEO-PPO diblocks for comparison, yielding similar results (Fig. S18 in Supporting information).

Specifically regarding 20% P407-$Zn(OTf)_2/H_2O$, Zn||Zn symmetric cells and Zn||Cu asymmetric cells were assembled to test the cycling stability and reversibility of the Zn anode in harsh environments. As shown in Fig. 4d, at 60 °C, the Zn||Zn symmetric cell with 20% P407-$Zn(OTf)_2/H_2O$ exhibited a lifespan of 850 h at 0.2 mA/cm^2 and 0.2 mAh/cm^2, while the cell with $Zn(OTf)_2/H_2O$ short-circuited after just 45 h of plating/stripping. Moreover, even at −30 °C, the Zn||Zn symmetric cell with 20% P407-$Zn(OTf)_2/H_2O$ maintained stable performance for 1000 h, while the $Zn(OTf)_2/H_2O$ cell failed after only 130 h (Fig. 4g). These results indicated that the introduction of P407 significantly enhanced the stability of the Zn anode under both standard and extreme conditions. To further assess the influence of P407 on reversibility, CE of Zn||Cu asymmetric cells was evaluated at both high and low temperatures. At

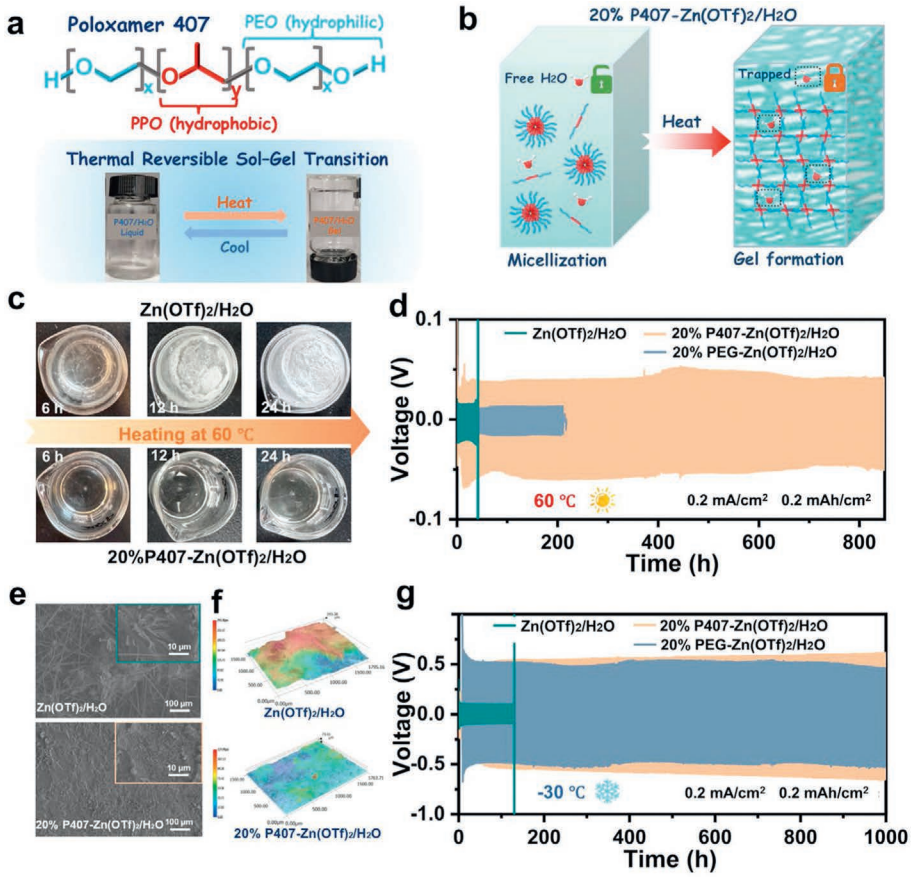


Fig. 4. Mechanism of P407-enhanced high-temperature stability. (a) The structure of poloxamer 407 and its thermal reversible property. (b) Diagram of physical states and H_2O dynamic behavior of 20% P407-$Zn(OTf)_2/H_2O$ electrolytes at 30 °C and 60 °C. (c) Digital images of $Zn(OTf)_2/H_2O$ and 20% P407-$Zn(OTf)_2/H_2O$ electrolytes after being heated at 60 °C for different durations. Long-term constant current cycling performance of Zn||Zn symmetric cells using three electrolytes at (d) 60 °C and (g) −30 °C. (e) SEM and (f) 3D digital microscopy images of Zn anodes after cycling in two electrolytes for 100 h at 1 mA/cm², 1 mAh/cm² and 60 °C.

60 °C, the CE of the cell with $Zn(OTf)_2/H_2O$ dropped sharply to 0 after 45 cycles (Fig. S19 in Supporting information), primarily due to severe side reactions such as HER, corrosion, and accelerated electrode-electrolyte interface polarization. Encouragingly, the cell with 20% P407-$Zn(OTf)_2/H_2O$ exhibited a much higher CE, maintaining an average CE of 92.0% over 80 cycles, with consistent voltage profiles at a current density of 0.4 mA/cm². Even at −30 °C, the cell with 20% P407-$Zn(OTf)_2/H_2O$ achieved CE of 93.8% over more than 500 plating/stripping cycles (Fig. S20 in Supporting information), with stable voltage profiles. These results indicated that the 20% P407-$Zn(OTf)_2/H_2O$ electrolyte exhibited excellent cycling stability and reversibility across a wide temperature range.

Subsequently, comparisons of the Zn anode surface morphology after 50 cycles at both high and low temperatures confirmed the beneficial effects of P407 (Figs. 4e and f, Figs. S21 and S22 in Supporting information). At 60 °C, SEM images of the Zn anode in $Zn(OTf)_2/H_2O$ exhibited significant dendrite growth, whereas the Zn anode in the 20% P407-$Zn(OTf)_2/H_2O$ electrolyte displayed a much more uniform surface. AFM and 3D microscopy also demonstrated a significant reduction in surface roughness of the Zn anode with the introduction of P407. Similar results were observed at −30 °C. Additionally, as shown in Fig. S23 (Supporting information), the XRD results further demonstrated that the P407-containing electrolyte facilitated preferential Zn deposition on the (002) crystal plane, which helped improve the performance of the Zn anode. In conclusion, the 20% P407-$Zn(OTf)_2/H_2O$ electrolyte showed excellent stability and adaptability across a wide temperature range. It improved Zn anode stability, reduced dendrite formation, enhanced reversibility, and ensured electrochemical stability. The introduction of P407 greatly boosted performance under both standard and extreme conditions, making it promising for advanced electrochemical applications.

Finally, to evaluate the practicality of the 20% P407-$Zn(OTf)_2/H_2O$ electrolyte in AZIBs, Zn-V_2O_5 full cells were assembled. As shown in Fig. S24 (Supporting information), cyclic voltammetry (CV) curves of Zn-V_2O_5 full cells using $Zn(OTf)_2/H_2O$ and 20% P407-$Zn(OTf)_2/H_2O$ electrolytes were measured at a scan rate of 0.1 mV/s. Both CV curves exhibited two pairs of redox peaks with similar shapes [44]. Subsequently, Zn-V_2O_5 full cells were tested across a wide temperature range. At 30 °C, the full cell with 20% P407-$Zn(OTf)_2/H_2O$ achieved a specific capacity of 114.2 mAh/g at 10 A/g, retaining 94.2% of capacity after 6000 cycles (Fig. 5a). In comparison, the cell with $Zn(OTf)_2/H_2O$ exhibited severe capacity decline after 1000 cycles, retaining only 31.9% after 6000 cycles due to Zn dendrite growth and persistent side reactions. As shown in Fig. 5b and Fig. S25 (Supporting information), the 20% P407-$Zn(OTf)_2/H_2O$ electrolyte also exhibited excellent rate performance, achieving discharge capacities of 231.9, 177.1, 148.3, 115.3, and 93.1 mAh/g at current densities of 0.5, 1, 2, 5, and 10 A/g, respectively. When the current density returned to 0.5 A/g, the capacity fully recovered, highlighting highly reversible Zn plating/stripping and rapid Zn^{2+} storage processes. The temperature adaptability of the full cell was further tested. At 60 °C, the full cell with 20% P407-$Zn(OTf)_2/H_2O$ maintained stable cycling for 1000 cycles at 5 A/g, with a capacity retention of 94.3% (Fig. 5c). In contrast, the $Zn(OTf)_2/H_2O$ cell failed after 300 cycles due to

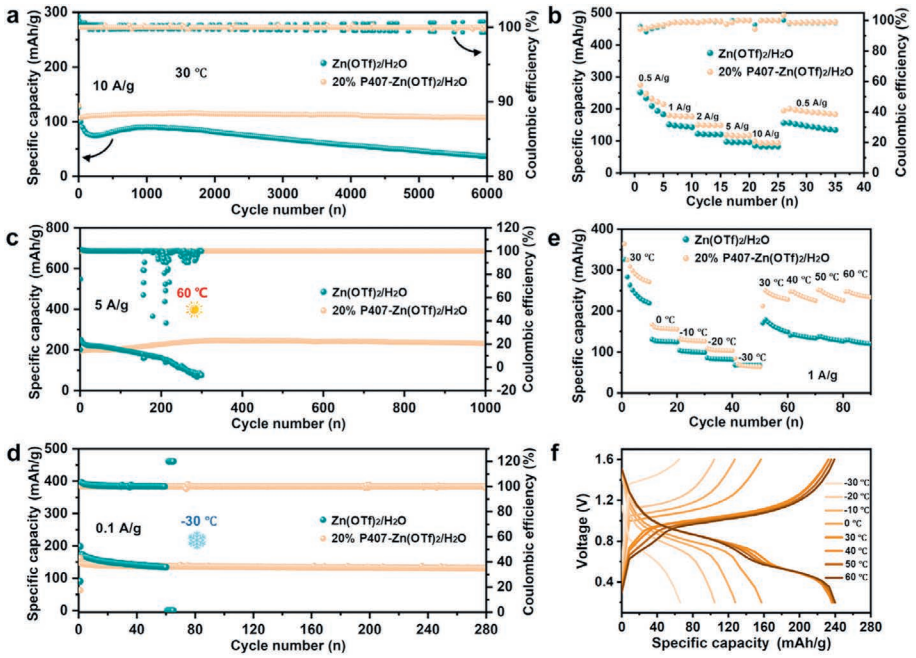


Fig. 5. Electrochemical performance of Zn-V_2O_5 full cells over a wide temperature range. (a) Cycling stability and CE of Zn-V_2O_5 full cells with two electrolytes at 10 A/g and 30 °C. (b) Rate performance of the Zn-V_2O_5 full cells with two electrolytes. Cycling stability and CE of Zn-V_2O_5 full cells with two electrolytes at (c) 5 A/g and 60 °C, and (d) 0.1 A/g and −30 °C. (e) Specific capacity of Zn-V_2O_5 full cells at 1 A/g under different temperatures. (f) Charge/discharge curves of the Zn||20% P407-Zn$(OTf)_2/H_2O$||V_2O_5 full cell at different temperatures.

accelerated Zn dendrite growth and aggravated side reactions. Even at −30 °C, the full cell with 20% P407-Zn$(OTf)_2/H_2O$ retained 90.3% capacity after 280 cycles, demonstrating excellent low-temperature performance (Fig. 5d). Additionally, the 20% P407-Zn$(OTf)_2/H_2O$ full cell exhibited remarkable capacity stability during temperature fluctuations. As the temperature decreased from 30 °C to −30 °C and then returned to 30 °C, the cell maintained stable capacity retention, fully recovering its capacity upon rewarming. Its capacity also increased with temperature, reaching ~240 mAh/g at 60 °C (Figs. 5e and f). In contrast, the Zn$(OTf)_2/H_2O$ full cell failed to recover its capacity after operation at low temperature and showed significant capacity degradation at higher temperature (Fig. S26 in Supporting information). These findings confirmed the superior adaptability of the 20% P407-Zn$(OTf)_2/H_2O$ electrolyte across extreme conditions. Its excellent thermal and freeze resistance, combined with improved Zn dendrite suppression and enhanced cycling stability, demonstrating its potential for advanced AZIBs applications over a broad temperature range (−30 °C to 60 °C).

In conclusion, P407 is introduced as an effective electrolyte additive to address the critical challenges associated with Zn anodes in AZIBs, offering a promising strategy for achieving wide-temperature performance. P407 facilitates the reconstruction of the solvation structure and regulation of H_2O cluster behavior, enabling the *in situ* formation of a stable and highly conductive organic-inorganic hybrid SEI layer on the Zn anode surface. This approach promotes uniform Zn deposition, suppresses dendrite growth, and effectively mitigates H_2O-related side reactions, thereby stabilizing the Zn-electrolyte interface. Additionally, the thermoreversible gelation property of P407 provides dual benefits: at high temperature, its crosslinked network structure retains H_2O molecules and minimizes evaporation, while at low temperature, it transitions to a liquid state to ensure efficient ion transport. With the modified electrolyte, Zn||Zn symmetric cell achieves stable cycling for over 4000 h, and Zn||Cu asymmetric cell exhibits a CE of up to 99.2% at 30 °C. Additionally, Zn-V_2O_5 full cell demonstrates excellent cycling stability and capacity retention across a wide temperature range from −30 °C to 60 °C. This study presents an innovative additive formulation that not only significantly enhances the interfacial stability and practicality of AZIBs but also provides valuable insights into the development of wide-temperature, high-performance aqueous energy storage systems. Moreover, this strategy shows strong potential for application in other wide-temperature aqueous metal-ion batteries, paving the way for the broader adoption of aqueous rechargeable energy storage technologies.

Declaration of competing interest

The authors declare that they have no known competing financial interests or personal relationships that could have appeared to influence the work reported in this paper.

CRediT authorship contribution statement

Xiaoxi Zhao: Writing – original draft, Methodology, Formal analysis, Data curation, Conceptualization. **Qingyun Dou:** Writing – review & editing, Supervision, Resources, Methodology, Funding acquisition, Conceptualization. **Bingjun Yang:** Writing – review & editing, Supervision, Funding acquisition. **Qunji Xue:** Resources. **Xingbin Yan:** Supervision, Resources, Funding acquisition.

Acknowledgments

This work was supported by the Guangdong Basic and Applied Basic Research Foundation (No. 2024A1515010158); the Guangzhou Science and Technology Programme (No. 2024A04J4281); the Young Talent Support Project of Guangzhou Association for Science and Technology; Gansu Provincial Key R&D Program Project-Industrial Projects (No. 24YFGA010) and the Western Young Scholars Foundations of Chinese Academy of Sciences.

Supplementary materials

Supplementary material associated with this article can be found, in the online version, at doi:10.1016/j.cclet.2025.110952.

References

[1] M. Chen, Y. Gong, Y. Zhao, et al., Nat. Sci. Rev. 11 (2024) nwae205.
[2] Y. Yin, X. Li, Renewables 1 (2023) 622–637.
[3] Q. Dou, N. Yao, W.K. Pang, et al., Energy Environ. Sci. 15 (2022) 4572–4583.
[4] Y. Wang, Z. Wang, W.K. Pang, et al., Nat. Commun. 14 (2023) 2720.
[5] X. Hu, Z. Zhao, Y. Yang, et al., InfoMat 6 (2024) e12620.
[6] Y. Sun, H. Ma, X. Zhang, et al., Adv. Funct. Mater. 31 (2021) 2101277.
[7] X. Zeng, S. Zhang, T. Long, et al., Renewables 2 (2024) 52–60.
[8] M. Chen, S. Xie, X. Zhao, et al., Energy Storage Mater 51 (2022) 683–718.
[9] S. Liu, R. Zhang, J. Mao, et al., Sci. Adv. 8 (2022) eabn5097.
[10] Y. Wang, L. Mo, X. Zhang, et al., Adv. Energy Mater. 14 (2024) 2402041.
[11] T. Xue, Y. Mu, X. Wei, et al., Carbon Neutral. 4 (2024) e183.
[12] C. Liu, X. Xie, B. Lu, et al., ACS Energy Lett. 6 (2021) 1015–1033.
[13] Q. Zhang, Y. Ma, Y. Lu, et al., Nat. Commun. 11 (2020) 4463.
[14] S. Cai, X. Chu, C. Liu, et al., Adv. Mater. 33 (2021) 2007470.
[15] T. Liang, R. Hou, Q. Dou, et al., Adv. Funct. Mater. 31 (2021) 2006749.
[16] X. Wang, X. Li, H. Fan, et al., Nano-Micro Lett. 14 (2022) 205.
[17] H. Ge, X. Xie, X. Xie, et al., Energy Environ. Sci. 17 (2024) 3270–3306.
[18] Y. Han, Y. Liu, Y. Zhang, et al., Adv. Mater. 37 (2024) 2412447.
[19] Q. Dou, S. Lei, D.W. Wang, et al., Energy Environ. Sci. 11 (2018) 3212–3219.
[20] X. Zhang, Y. Liu, S. Wang, et al., Energy Storage Mater. 70 (2024) 103471.
[21] Y. Qiu, X. Zheng, R. Zhang, et al., Adv. Funct. Mater. 34 (2024) 2310825.
[22] R. Wang, Q. Ma, L. Zhang, et al., Adv. Energy Mater. 13 (2023) 2302543.
[23] J. Wan, R. Wang, Z. Liu, et al., Adv. Mater. 36 (2024) 2310623.
[24] G. Qu, H. Wei, S. Zhao, et al., Adv. Mater. 36 (2024) 2400370.
[25] L. Liu, Y. Liu, L. Zhang, et al., Energy Fuels 38 (2024) 15998–16009.
[26] J. Zhang, C. Lin, L. Zeng, et al., Small 20 (2024) 2312116.
[27] S. Zhao, Y. Zuo, T. Liu, et al., Adv. Energy Mater. 11 (2021) 2101749.
[28] Q. Zhang, K. Xia, Y. Ma, et al., ACS Energy Lett. 6 (2021) 2704–2712.
[29] G. Yang, J. Huang, X. Wan, et al., EcoMat 4 (2022) e12165.
[30] R. Hou, S. Guo, H. Zhou, Adv. Energy Mater. 13 (2023) 2300053.
[31] E. Giuliano, D. Paolino, M. Fresta, et al., Pharmaceutics 10 (2018) 159.
[32] D. Han, T. Sun, R. Zhang, et al., J. Energy Chem. 32 (2022) 2209065.
[33] D. Guo, J. Wang, T. Lai, et al., Adv. Mater. 35 (2024) 2300841.
[34] Z. Xie, N. Chen, M. Zhang, et al., ACS Energy Lett. 9 (2024) 3380–3390.
[35] Y. Li, J. Cheng, D. Zhao, et al., Energy Storage Mater. 63 (2023) 102997.
[36] R. Zhang, W.K. Pang, J.P. Vongsvivut, Energy Environ. Sci. 17 (2024) 4569–4581.
[37] Y. Dong, L. Miao, G. Ma, et al., Chem. Sci. 12 (2021) 5843–5852.
[38] B. Niu, Z. Li, D. Luo, et al., Energy Environ. Sci. 16 (2023) 1662–1675.
[39] Q. Ren, X. Tang, X. Zhao, et al., Nano Energy 109 (2023) 108306.
[40] C. Chang, S. Hu, T. Li, et al., Energy Environ. Sci. 17 (2024) 680–694.
[41] K. Roy, A. Rana, T.K. Ghosh, et al., Adv. Energy Mater. 14 (2024) 2303998.
[42] Z. Wang, J. Diao, J.N. Burrow, et al., Adv. Funct. Mater. 34 (2024) 2311271.
[43] Y. Chen, J.H. Lee, M. Meng, et al., Materials 14 (2021) 4522.
[44] N. Zhang, Y. Dong, M. Jia, et al., ACS Energy Lett. 3 (2018) 1366–1372.